AIP | Applied Physics Letters

Solid phase epitaxy of ultra-shallow Sn implanted Si observed using high-resolution Rutherford backscattering spectrometry

T. K. Chan, F. Fang, A. Markwitz, and T. Osipowicz

Citation: Appl. Phys. Lett. **101**, 081602 (2012); doi: 10.1063/1.4747487
View online: http://dx.doi.org/10.1063/1.4747487
View Table of Contents: http://apl.aip.org/resource/1/APPLAB/v101/i8
Published by the American Institute of Physics.

Related Articles

High phosphorous doped germanium: Dopant diffusion and modeling
J. Appl. Phys. 112, 034509 (2012)

Understanding Si(111) solid phase epitaxial regrowth using Monte Carlo modeling: Bi-modal growth, defect formation, and interface topology
J. Appl. Phys. 112, 024327 (2012)

Room temperature sub-bandgap photoluminescence from silicon containing oxide precipitates
Appl. Phys. Lett. 101, 032107 (2012)

Spatial-temporally resolved high-frequency surface acoustic waves on silicon investigated by femtosecond spectroscopy
Appl. Phys. Lett. 101, 013108 (2012)

Simultaneous flattening of Si(110), (111), and (001) surfaces for three-dimensional Si nanowires
Appl. Phys. Lett. 100, 261605 (2012)

Additional information on Appl. Phys. Lett.

Journal Homepage: http://apl.aip.org/
Journal Information: http://apl.aip.org/about/about_the_journal
Top downloads: http://apl.aip.org/features/most_downloaded
Information for Authors: http://apl.aip.org/authors

ADVERTISEMENT

Solid phase epitaxy of ultra-shallow Sn implanted Si observed using high-resolution Rutherford backscattering spectrometry

T. K. Chan,[1] F. Fang,[2] A. Markwitz,[2] and T. Osipowicz[1]
[1]*Centre for Ion Beam Applications, Department of Physics, National University of Singapore, Blk S12, 2 Science Drive 3, Singapore 117551*
[2]*National Isotope Centre, GNS Science, 30 Gracefield Road, Gracefield 5010, P.O. Box 31-312, Lower Hutt 5040, New Zealand*

(Received 18 June 2012; accepted 8 August 2012; published online 21 August 2012)

We present detailed observations of the solid phase epitaxy process in Sn-implanted Si samples with nanometric depth resolution within a 50 nm ultra-shallow region beneath the surface. Measurements were made using high-resolution Rutherford backscattering spectrometry coupled with the ion channeling technique. Samples with Sn ions implanted onto Si substrates with and without prior Si^+ self-amorphization implantation process show different crystal regrowth characteristics during annealing. Regrowth proceeds at a non-uniform rate up to a certain depth before stopping, and an Arrhenius-type defect density limiting model of crystal regrowth is proposed to account for this effect. © *2012 American Institute of Physics*. [http://dx.doi.org/10.1063/1.4747487]

The process of solid phase epitaxy (SPE) has been subject of research for several decades, due to its applications in Si device manufacturing. However, the exact mechanism of crystal regrowth by SPE is yet unknown. The factors which influence the SPE process have been well established over the years: annealing temperature, impurity species, implantation dose and dose rate, lattice strain, types of dopants, and substrate orientation.[1] Current research is mainly focused on the details of defect accumulation and elimination mechanisms. Large and complex computer simulations of the SPE and amorphization processes have become possible and were carried out very recently in order to identify the types of defects responsible for amorphization,[2,3] which then determines the characteristics of their dissolution during SPE. On the experimental side, to date, there is still no consensus on the exact defect types and the mechanisms of their accumulation during amorphization and SPE, as definitive direct experimental observation of the defects produced by ion irradiation proved rather difficult.[4] In this paper, we present results on the behavior of SPE process induced by electron beam annealing (EBA) for ion implantation in Si substrates with and without a prior Si^+ self-amorphizaion (SA) process.

Group IV semiconductor alloys are interesting for their potential applications in optoelectronic devices capable of monolithic integration with existing Si circuitry,[5] as well as source/drain stressors in metal oxide semiconductor transistors.[6,7] In recent years, the continuing downscaling of devices has caused the transistor junction depth, along with the source/drain thickness to reach the regime of 20 nm or less. As such, ultra-shallow ion implantation has become necessary, and it is important to understand the kinetics of SPE in such a thickness regime. However, no detailed study of the SPE process in such ion-implanted ultra-shallow depths has yet been made, largely due to limitations in detection resolution. In this paper, measurements were made on Sn implanted Si using high-resolution Rutherford backscattering spectrometry (HRBS) in an ultra-shallow region of less than 40 nm in thickness. The energy resolution of our HRBS measurements is ~1 keV with 500 keV He^+ beams, which gives a depth resolution of ~1 nm in Si and ~5 Å in heavy elements. This allows for a meaningful and detailed analysis of the Sn implantation depth profiles and the subsequent SPE process for such ultra-shallow regions that is required for next generation semiconductor manufacturing processes.

Ion implantation and annealing of samples were performed at GNS Science New Zealand,[8] using identical n-type Si(100) substrates. For the samples without SA, Sn ions were implanted directly into the substrates, while the Si substrates of samples with SA were amorphized using 25 keV Si^+ ions at a fluence of 5×10^{14} cm^{-2} before the Sn implantations were performed. All Sn implantations were conducted with 20 keV Sn^+ ions at a fluence of 2×10^{15} cm^{-2} at room temperature under high vacuum with low beam currents (<5 $\mu A\,cm^{-2}$) to reduce heating effects. Annealing was subsequently performed *in situ* by raster scanning a focused, high intensity (3–4 mA) 20 keV electron beam over the implanted sample, with a ramp up and down temperature gradient of 5 °C s^{-1}. A peak temperature accuracy of ±1° was obtained using a computer-controlled feedback system tied to a two-color pyrometer. Three sets of samples were prepared: Sets A and B are samples prepared without and with SA process, respectively, with both sets subsequently annealed at a fixed temperature of 529 °C at different durations ranging from 50 s to 1000 s. Set C has been prepared with SA process and annealed at different temperatures ranging from 400 °C to 550 °C for a fixed duration of 500 s.

HRBS measurements were performed at the Centre for Ion Beam Applications at the National University of Singapore.[9] Samples were mounted onto a precision 5-axis goniometer within a scattering chamber maintained under ultra-high vacuum. A collimated beam of 500 keV He^+ ions generated using a 3.5 MV Singletron accelerator was incident onto the samples. Ions backscattered at 65° were measured by a detection system which consists of a 90° double focusing spectrometer magnet and a 1-D position sensitive focal plane detector coupled with a micro-channel plate stack for signal amplification. Aligned spectra were measured along the ⟨111⟩ channeling axis of the Si substrate.

Figs. 1(a) and 1(b) show the ⟨111⟩ aligned HRBS spectra for sets A and B respectively. Each spectrum represents a snapshot at different instants of time during the SPE process up to 1000 s during annealing. The signals from Sn, Si, and O are clearly visible in the spectra, their surface energies are indicated. For both sets, the amorphous/crystalline (a/c) interface within the substrate is clearly seen to sweep towards the surface with increasing annealing duration and stops at a depth of ~20 nm by 500 s of annealing in both sets of samples. The depth scale in each spectrum also clearly shows the nanometric depth resolution of HRBS. Re-

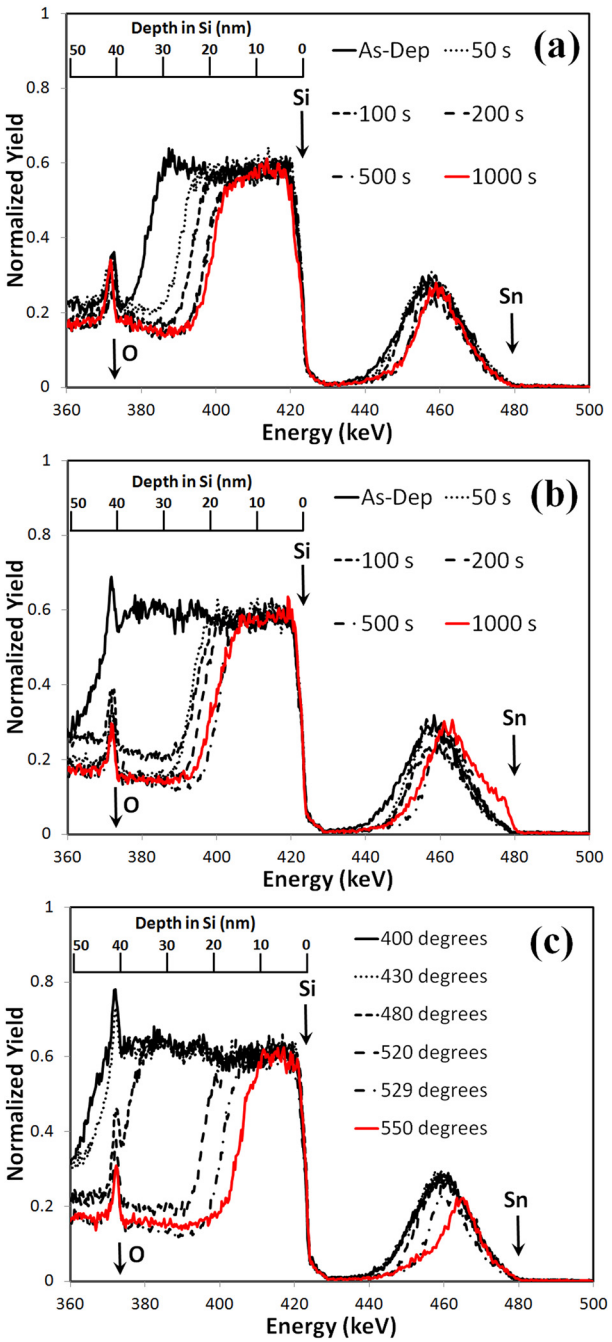

FIG. 1. ⟨111⟩ aligned spectra for (a) set A without SA, (b) set B with SA and (c) set C with SA. Sets A and B were annealed for various durations at a fixed temperature of 529 °C while set C was annealed at various temperatures for a fixed duration of 500 s. Depth scales in the spectra show the variation of the thicknesses of the remaining damaged Si layer at the various annealing durations and temperatures.

distribution of Sn is detected in set B by 1000 s of annealing and at the same time the roughness of the a/c interface is seen to increase. However, neither movement of Sn nor roughening of a/c interface is seen in set A by 1000 s of annealing. Fig. 1(c) shows the ⟨111⟩ aligned spectra for set C, where samples with SA were annealed at different temperatures for a fixed duration of 500 s. Here, no movement of Sn is detected for all temperatures, and the position of a/c interface by 500 s of anneal approaches the surface progressively with increasing temperature.

It is well known that random nucleation crystallites may occur in amorphous Si during annealing which leads to polycrystalline Si formation. A melt-induced model proposed by Thornton *et al.*[10] assumes that the Sn will form mobile melts during annealing due to its low melting point. If there is crystallite nucleation, Si concentration gradients are set up across the Sn melt droplets due to a higher dissolution rate of amorphous Si into the melt as compared to crystalline Si, causing Sn melts to move within amorphous Si and leave behind trails of polycrystallites. This may also be responsible for the a/c interface roughening as well as the movement of Sn in set B, where the mobile Sn melts move both towards the surface as well as deeper into the sample where they encounter the a/c interface. Eventually, the interface becomes a polycrystalline/crystalline interface. The implantation of Sn into crystalline Si in set A and amorphous Si in set B may give rise to different defect types which in turn affects the properties of the random nucleation process. This may be the reason for the absence of polycrystallite nucleation and Sn movement in set A.

Using the SIMNRA simulation program,[11] Sn depth profiles were extracted from the random spectra (not shown), while depth positions of the a/c interface were extracted from each aligned spectrum. The Monte Carlo Dynamic-TRIM (T-DYN) program[12] was also used to simulate the expected vacancy defect density and the implantation profiles within the substrates resulting from both the SA and Sn implantation processes. Fig. 2(a) shows the depth position of the a/c interface at different instances of time for sets A and B, as well as at different annealing temperatures for set C. For sets A and B, the SPE process appears to proceed in a highly non-uniform manner, with the a/c interface moving with the highest velocity within the first 50 s of the anneal and rapidly slowing down with increasing duration. Most of the SPE process was completed by 200 s and by 500 s, the a/c interface for both sets appear to have stopped at a depth of about 20 nm, up to 1000 s of annealing.

Fig. 2(b) shows the T-DYN results for the total number of defect vacancies produced by the SA and implantation processes per nm of depth, as well as the experimental depth profiles of as-implanted Sn extracted from SIMNRA. Such a calculation of the total number of vacancies generated per nm should directly reflect the actual defect density profile within each sample. From these results, the Sn implantation process is seen to generate a massive, sharply peaked damage profile up to a depth of about 35 nm, while the Si SA process generates a broad, relatively low-level damage up to 80 nm in depth.

Since SPE is a process of defect dissolution, its rate depends on the defect type. For instance, Tang *et al.*[13] have

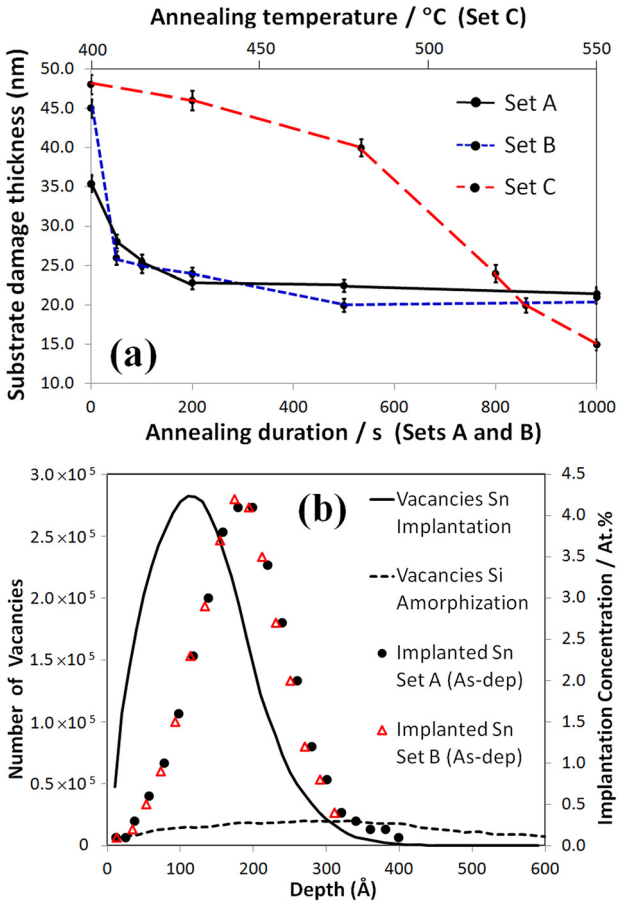

FIG. 2. (a) Depth position of a/c interface at different annealing durations at 529 °C (sets A and B, bottom abscissa) and at different annealing temperatures for 500 s (set C, top abscissa), (b) Dynamic TRIM simulation of vacancies and actual implantation profiles extracted from SIMNRA fits.

proposed a metastable Interstitial–vacancy (IV) pair defect as the amorphization defect, while Pelaz *et al.*[14] extended the concept into different dissolution rates for different IV pair densities where extended clusters of IV pairs produced by heavy ion implantation require a much higher activation energy (and duration) for dissolution as compared to isolated IV pair defects produced by light ions. The as-deposited sample of set B with SA has a damage region of only 45 nm as compared to 80 nm of damage from T-DYN results, suggesting that the SA process produces isolated IV pairs and other simple defects which are partially annealed out dynamically during the SA and Sn implantation processes. The heavy Sn implantation, however, created IV pair clusters (among other extended defects) that are not as readily dissolved. This manifests in our results as an absence in a dynamic annealing effect in the set B as-deposited sample, and also in that the a/c interface for both sets stops at 20 nm below the surface.

The velocity of SPE has conventionally been assumed to follow an Arrhenius-type behavior, where a single value of SPE rate v is assigned to each annealing temperature T. However, our results show that the SPE rate is highly non-uniform, with large initial SPE rates that rapidly decrease with annealing duration. This is due to the large changes in the defect density with depth, caused by the sharply peaked damage profile generated by Sn implantation (or by any other type of heavy ion at a single energy). In such cases, annealing at the same temperature will result in a range of regrowth rates at different instances during annealing, and the usual Arrhenius plot of regrowth rate vs annealing temperature becomes meaningless. Here, we propose a model where every annealing temperature T is instead related to the upper limit of defect density D_{lim} beyond which SPE may no longer proceed, also in an Arrhenius-type behavior

$$D_{\mathrm{lim}} = D_0\, e^{-E_a/k_B T},$$

where D_0 is the pre-factor and E_a is the activation energy. This is not limited to Sn implanted Si, but applies to all other ion-implanted samples with non-uniform defect density profiles with depth. However, different defect types or cluster morphologies might give rise to different E_a, with simple defects expected to yield a smaller value.

We apply our model to the data for set C samples. The limit D_{lim} in terms of total vacancy number per nm of depth is extracted from the T-DYN results in Fig. 2(b) at the a/c interface depth positions for each T data point of set C in Fig. 2(a). Samples with $T < 480\,^{\circ}\mathrm{C}$ have a/c interface positions at >40 nm in depth which is due to SA process alone. This region may have different defect types as depth regions <40 nm for $T \geq 480\,^{\circ}\mathrm{C}$ where defect density generated by Sn implantation dominates. Hence we limit our data to $T \geq 480\,^{\circ}\mathrm{C}$ for our model.

The Arrhenius plot for our model is shown in Fig. 3. Results show a good agreement between the data and our model, with the activation energy E_a calculated to be 2.1 eV. In particular, the sample where $T = 550\,^{\circ}\mathrm{C}$ allows for a D_{lim} that is very nearly at the top of the Sn damage peak. Therefore, at a larger T, the SPE process will not be expected to stop, and the a/c interface will reach the surface. Indeed, samples annealed at 629 °C (not shown) indicate complete SPE right up to the surface.

Electronic effects such as dopants and structural effects such as lattice strain are known to modify the SPE rate. In particular, drastic reduction in SPE rate has been attributed to lattice strain due to local bond distortions caused by the incorporation of impurity atoms into substitutional sites.

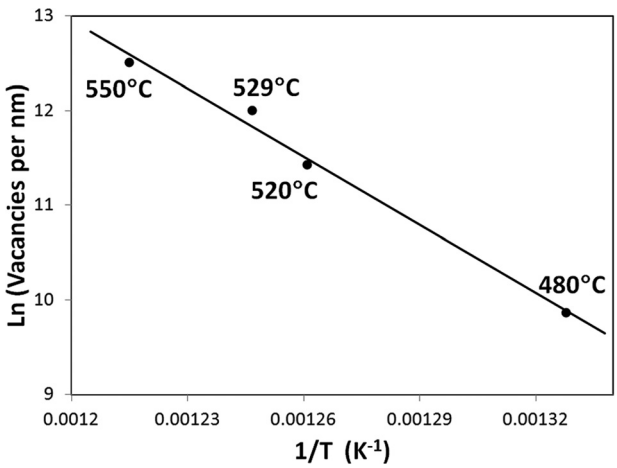

FIG. 3. Arrhenius plot of Log (D_{lim}) vs $1/T$ for samples in set C where $T \geq 480\,^{\circ}\mathrm{C}$.

However, our model assumes that SPE regrowth is stopped by a defect density barrier at the very end of the process and does not address the effects of SPE rate modification prior to reaching D_{lim}. Indeed, the good agreement between results from set C and our model for our Sn implantation dose and range of annealing temperatures suggests that the limit D_{lim} is not affected by such effects. Our model hence serves to unify the separate characteristics of SPE due to different implantation of ion species, dose, and dose rate into a process dependent only on annealing temperature, defect types, and densities. Note that for large implantation doses, complex types and cluster morphologies of defects may form at very high defect density regions, causing deviations from our model.

In conclusion, a detailed observation of the SPE process within an ultra-shallow region of less than 50 nm beneath the surface was conducted using HRBS at nanometric depth resolution. A highly non-uniform SPE rate was observed during annealing and SPE stops at a particular depth beneath the surface for each annealing temperature. A model was proposed where the SPE process is viewed as being able to proceed only in regions containing a density of defects up to a certain limit at each annealing temperature. Such a model may serve to unify the various limiting behaviors during SPE while using different ion species and at different dose and dose rates. It may also serve to provide for a tighter control over the ion implantation and the subsequent annealing processes during the fabrication of next generation devices.

[1]D. T. J. Hurle, *Handbook of Crystal Growth* (Elsevier Science, North-Holland, 1994), Vol. 3, p. 255.
[2]E. Lampin and C. Krzeminski, J. Appl. Phys. **106**, 063519 (2009).
[3]I. Martin-Bragado, Appl. Phys. Lett. **98**, 233109 (2011).
[4]P. D. Edmondson, D. J. Riley, R. C. Birtcher, and S. E. Donnelly, J. Appl. Phys. **106**, 043505 (2009).
[5]J. Kouvetakis and A. V. G. Chizmeshya, J. Mater. Chem. **17**, 1649 (2007).
[6]G. H. Wang, E. H. Toh, X. Wang, S. Tripathy, T. Osipowicz, T. K. Chan, K. M. Hoe, S. Balakumar, G. Q. Lo, G. Samudra, and Y. C. Yeo, Appl. Phys. Lett. **91**, 202105 (2007).
[7]B. Vincent, Y. Shimura, S. Takeuchi, G. Eneman, A. Firrincieli, J. Demeulemeester, A. Vantomme, T. Clarysse, O. Nakatsuka, S. Zaima, J. Dekoster, M. Caymax, and R. Loo, Microelectron. Eng. **88**, 342 (2011).
[8]A. Markwitz, D. A. Carder, T. Hopf, J. Kennedy, T. K. Chan, A. Mücklich, and T. Osipowicz, Nucl. Instrum. Meth. B **273**, 199 (2012).
[9]T. Osipowicz, H. L. Seng, T. K. Chan, and B. Ho, Nucl. Instrum. Meth. B **249**, 915 (2006).
[10]R. P. Thornton, R. G. Elliman, and J. S. Williams, J. Mater. Res. **5**, 1003 (1990).
[11]M. Mayer, AIP Conf. Proc. **475**, 541 (1999).
[12]J. P. Biersack, S. Berg, and C. Nender, Nucl. Instrum. Meth. B **59–60**(Part 1), 21 (1991).
[13]M. Tang, L. Colombo, J. Zhu, and T. Diaz de la Rubia, Phys. Rev B **55**, 14279 (1997).
[14]L. Pelaz, L. A. Marques, M. Aboy, J. Barbolla, and G. H. Gilmer, Appl. Phys. Lett. **82**, 2038 (2003).